Aerodynamic performances of rounded fastback vehicle

Giacomo Rossitto[1,2], Christophe Sicot[2], Valérie Ferrand[3], Jacques Borée[2] and Fabien Harambat[1]

Abstract

Experimental and numerical analyzes were performed to investigate the aerodynamic performances of a realistic vehicle with a different afterbody rounding. This afterbody rounding resulted in a reduction to drag and lift at a yaw angle of zero, while the crosswind performances were degraded. Rounding the side pillars generated moderate changes to the drag and also caused important lift reductions. A minor effect on the drag force was found to result from the opposite drag effects on the slanted and vertical surfaces. The vorticity distribution in the near wake was also analyzed to understand the flow field modifications due to the afterbody rounding. Crosswind sensitivity was investigated to complete the analysis of the aerodynamic performances of the rounded edges models. Additional tests were conducted with geometry modifications as spoilers and underbody diffusers.

Keywords

Rounded edges, drag, vorticity, wake analysis, crosswind, spoilers, underbody diffuser

1 Introduction

For the last decade car manufacturers have been facing the challenging task of reducing fuel consumption and CO_2 emissions. In response to this, optimization algorithms have been applied to generate new vehicle shapes to minimize the aerodynamic drag. Since the obtained optimum shapes have no brand differentiating details, nowadays stylists are trying to give back a brand signature by proposing "non-conventional shapes. In that framework, the important rounding of the rear pillars becomes a differentiation strategy. The current study suggests to quantify the influence of such afterbody rounding on the flow field and on the drag development over a fastback vehicle.

Very few papers have addressed the question of the curvature of the rear edges in aerodynamic vehicle performances. One of the first works was presented by Gilhaus et al.[1] and Howell.[2] Thanks to balance measurements, it was found that rounded pillars reduced both drag and rear lift but yawing moment had a pronounced increase. Only recently, were advanced techniques used to achieve better understanding of the afterbody rounding. Thacker et al.[3] showed that rounding the edge between the roof and the rear slant of the Ahmed body results in a 10% drag reduction. Authors attributed this reduction to the fully attached flow over the backlight and the downstream shift of the rotating structures developing in the near wake. Fuller et al.[4] analyzed the benefits of rounding the rear side pillars on the Davis model. They observed that rounded edges generate a different wake structure dominated by the interaction between the longitudinal vortices and the separated region. The rounded edges model resulted in a drag and lift reduction of 11% and 25% respectively. The impact of afterbody rounding was mentioned also during the development of the Tesla Model S by Palin et al.[5] Important curved side pillars were avoided to reduce the highly dynamic wake, which caused large variation in the base pressure.

From the literature review, it appears that rounding afterbodies considerably affects the aerodynamic loads and flow development, but a systematic investigation into the effects of changing the radii of the side

[1]PSA Groupe, Velizy–Villacoublay, France
[2]Institut Pprime, UPR-3346 CNRS, ENSMA, Université de Poitiers, France
[3]Institut Supérieur de l'Aéronautique et de l'Espace (ISAE-SUPAERO), Université de Toulouse, France

Corresponding author:
Giacomo Rossitto, PSA Groupe, Centre Technique Velizy A, Velizy - Villacoublay, France.
Email: giacomo.rossitto@ensma.fr

backlight edges was not reported. To complement the recent study proposed by the same authors[6] over a simplified car model (Ahmed body), the present study addresses this question on a realistic car model equipped with various rear pillars curvatures. Special care is taken to understand how the modified flow on the backlight interacts with the near wake and how this promotes drag and lift changes.

Four rear ends were analyzed by combining PIV data to balance surface pressure measurements to fully characterize the flow structures and the associated aerodynamic forces. The zero yaw case was first explored before focusing on the crosswind effects. Complementary numerical simulations were systematically applied to complete the experimental data and to help the physical analysis. Geometry modifications, by means of spoilers and underbody diffusers, were investigated to understand their sensitivity to the side edges rounding.

2 Experimental and numerical set-up

The model and its relevant dimensions are reported in Figure 1. Four rear ends are tested; they differ by their side pillars curvature. The curvature radius is given as a percentage of the model span, i.e. 300 mm. The model equipped with sharp pillars having 0% radius is referred to as S_0 and it is considered as the reference case. The others models are S_8, S_{20}, and S_{40}. All of the rear ends have the same curvature at the end of the roof to avoid flow separation. The corresponding radius is chosen to maximize the room for the rear passengers for a fixed backlight angle of 23 degrees. The model features a realistic non symmetric underbody with an exhaust line. It does not have open front air intake. The horizontal projection of the slanted surface, $\xi = 440$ mm, will be used as a reference length. Starred spatial coordinates are normalized by the reference length.

The experimental results reported in this work were obtained from tests conducted in the PSA Groupe wind tunnel of La Ferté Vidame. The Eiffel wind tunnel is 52 meters long and has a test section which is 2 meters high, 5.2 meters wide and 6 meters long. It has a maximum free stream velocity of 53 m/s. The wind tunnel blockage ratio was 1.4%. The wind tunnel experiments were conducted with a fixed ground and the model is placed over a false floor. All of the data were obtained at 40 m/s which gives a Reynolds number based on the length of the model of 2.6e6. Starred velocities are normalized by the free stream velocity. A six components balance was used to measure the aerodynamic forces acting on the model. The drag and lift coefficients were calculated as follows

$$C_{d,l} = \frac{F_{d,l}}{\frac{1}{2}\rho U_0^2 S}$$

where F is the force measured by the balance, ρ the density of the air, and S the frontal surface area of the model. The precision of the balance was 0.001 for the drag coefficient Cd and 0.002 for the lift coefficient Cl.

Static surface pressure was recorded by 40 pressure probes over the vertical surface of the rear end. Thirty-five probes were located on the driver side and the rest were located on the passenger side to check the symmetry of the static surface pressure over the vertical base. Even thought the non-symmetric underbody should have induced asymmetry in the flow the comparison between the pressure probes, not reported here for brevity, resulted in negligible differences. Those probes were connected to a SCANdaq 8000 acquisition system. The acquisition rate was 40 Hz for 3000 samples giving 75 s of time recording. The static surface pressure coefficient at one point i was computed from the expression

$$C_P(i) = \frac{P(i) - P_0}{\frac{1}{2}\rho U_0^2}$$

where $P(i)$ is the static pressure of point (i), P_0 the static pressure measured upstream of the model. The static accuracy of the system is ± 13 Pa, i.e. 0.015 Cp.

Furthermore, PIV measurements were performed in the wake of the model. The laser sheet was set by a 2*120 mJ Nd:Yag Quantum Big Sky Laser. The Dantec Flowsense 4M mkII camera (2024 pixels by 2024 pixels) was equipped with 105 mm lenses which generated a 462 mm by 462 mm field of view. 2D PIV was performed on the symmetry (x,z) plane $Y^* = 0$. For all the PIV measurements, post-processing was performed with a final interrogation window of 16*16 pixels, after an initial window of 32*32 pixels, with an overlap of 50% in horizontal and vertical directions. The grid spacing was 1.82 mm. An SNR filter was applied to remove vectors with SNR < 1.2. 900 images were recorded with a 7 Hz trigger rate. With this setting, the 95% confidence limit represents approximately $\pm 3\%$ of the mean velocity.[7]

The numerical simulations presented in this work were computed with the commercial code *PowerFLOW*© (version 5.0c) based on the lattice Boltzmann model. Applications of the lattice

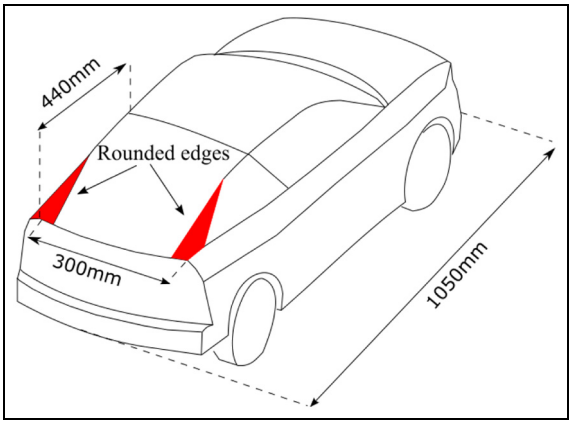

Figure 1. Fastback vehicle model and location of the rounded edges.

Table 1. Numerical *PowerFLOW*© setting.

Physical Time Scaling	1 timestep = 9.308×10^{-6} s
Minimum Level of VR	VR 9 (2.50×10^{-3} m/voxel)
Simulation time	324,000 timesteps (3 s)
Reynolds	1.04402×10^{7}

Boltzmann method to vehicles aerodynamics can be found in the literature.[8,9] The simulation setting is reported in Table 1. The model size for the numerical simulations corresponds to a real vehicle scale. At Reynolds 1.04e7, 324,000 time-steps were computed (3 seconds of real time). Local variable refinement regions VRs were defined to locally allow the coarsening of the grid by a factor of 2 starting from the Minimum Level of VR.[8] The minimum value of VR (Table 1) corresponds approximately to 300 wall units. The computational grid consisted of 1.2 million volume elements and 0.6 million surface elements. The computational domain was chosen according to PSA methodology. The model is positioned 17.5L from the domain inlet and the total length of the computational domain is 35L (L is the model length). In the following, temporally averaged velocity and pressure fields will be shown. These averages are computed over approximately 25 convective time scales L/U_0 where U_0 is the external velocity.

This setting allowed for agreements between the numerical and experimental results, as it is possible to examine in Figure 3 which reports a comparison of mean streamwise velocity profiles.

3 Base geometry flow analysis

This section analyzes the mean properties of the flow field modifications due to afterbody rounding. First, the zero yaw flow field and forces are analyzed. At the second stage, the crosswind performances are investigated.

Table 2 reports the variation of aerodynamic coefficients and the averaged base pressure with respect to the reference case S_0. Increasing the side radius generates a small drag reduction and a significant lift reduction. For the S_0 configuration, most of the rear lift is generated over the rear end by the low value of the pressure over the curved roof edge and from the low pressure foot-print of the longitudinal vortices, the so-called C-pillar vortices. These vortices are generated by the interaction between the flow coming from the side of the model and the flow over the rear window. Since the roof radius is constant among the four models, lift reductions are caused by the C-pillar vortices intensity modifications due to side rounding.

For a moderate value of C-pillars rounding, the origin of the longitudinal vortices is displaced towards the base of the body along the C-pillars.[6] For larger rounding, three-dimensional flow separation does not occur anymore on the side of the model and thus the side vortices disappear.[10] The weakening of the C-pillar vortices allows for a pressure recovery over the rear window reducing its contribution to drag and lift. However, the variation of the average base pressure over the vertical surface, reported in Figure 2 and in Table 2, gives evidence that the base pressure is reduced when the curvature side radius is increased. For S_{40}, the base pressure is 17% lower than for S_0, resulting in an important local drag increase. This effect counter-balances the local drag reduction of the rear window and can explain the weak effect of the pillars rounding on the global drag (Table 2).

The mean velocity fields in the symmetry plane are reported in Figure 4. It was chosen not to report the intermediate configurations, i.e. S_8 and S_{20}, to focus on the main differences between the most rounded rear pillar model S_{40} and the sharpest one S_0. The symmetry plane is far from sufficient to describe the entire topology of the tridimensional near wake, nevertheless it is very useful to get a first hint of the changes made by side rounding. Over the rear window, no major differences are noticed between the two models. The flow is attached to the slanted surface due to the important roof radius for both models. For S_0, the average separated zone in the close wake is characterized by two counter-rotating structures. The mean recirculating length, identified by the saddle point of the 2D mean streamlines, is at X* = 0.33 and X* = 0.23 respectively for S_0 and S_{40}. Adding pillar curvature reduces the

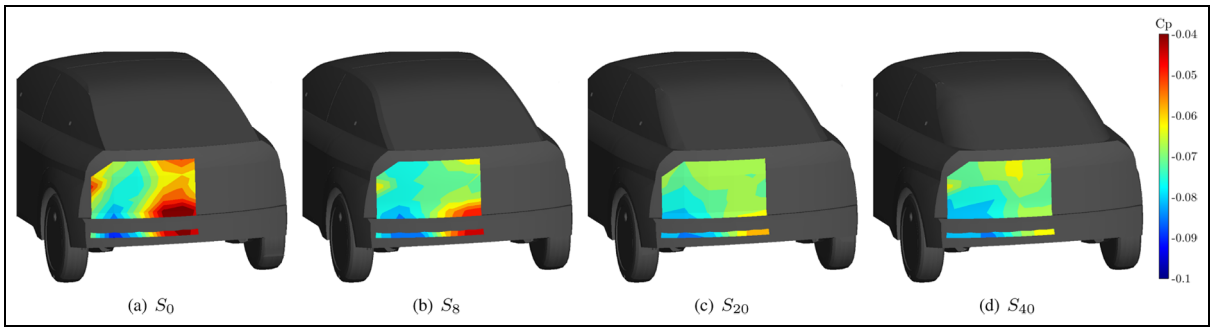

Figure 2. Experimental surface pressure coefficient distribution over the vehicle base.

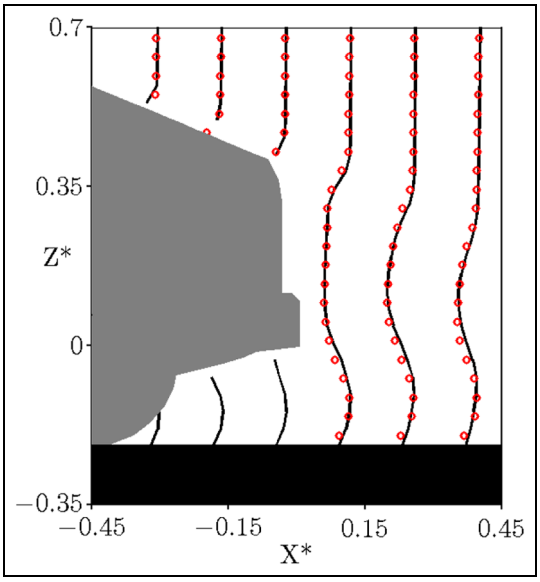

Figure 3. Comparison between numerical and experimental results. Mean streamwise velocity profiles. ° Experimental, – Numerical.

Table 2. Variation of aerodynamic coefficients and averaged base pressure relative to S_0.

	ΔCd	ΔCl	ΔCp base
S_0	-	-	-
S_8	0%	−13%	−12%
S_{20}	−1.5%	−18%	−15%
S_{40}	−2%	−27%	−17%

length of the near wake and modifies the topology of the enclosed structures. For S_{40}, the mean curvature of the near wake is increased due to the negative normal velocity. Regarding the flow organization inside the near wake, the upper structure is not evidenced anymore and the lower structure seems to be reduced. Such a strong modification of the near wake properties in the symmetry plane, may result from a 3D modification of the flow field due to side rounding.

To understand this complex mechanism, cross-flow planes are displayed in Figure 5. The data are issued from the numerical simulations. Each picture is divided in two: the left side represents S_0 and the right side S_{40}. At X* = 0.02, right after the rear slant, the longitudinal vorticity ($\Omega_{x*} = \frac{\Omega_{x*\xi}}{U_0}$) is concentrated in the C-pillar vortex for S_0 (left part of top of Figure 5). At the same X plane, a diffuse horizontal small area of longitudinal vorticity is present for S_{40} located in the shear layer (right part of top of Figure 5). Two-dimensional lines tangent at each point to the vector (V,W) are also drawn in Figure 5 to underline the different organization of flow fields due to the afterbody rounding. At X* = 0.23, i.e. the S_{40} saddle point location, the overall longitudinal rotation of the S_{40} near wake is showed in the bottom of Figure 5. The high spanwise and vertical velocity associated to the transversal flow in S_{40}, therefore, results in a global longitudinal rotation of the flow in the near wake. To quantify the rotation of the flow, the longitudinal evolution of the mean circulation $\Gamma* = \int_{S*} \Omega_x^* dS$ was analyzed as in the work of Rossitto et al.[6] The domain of the calculation included all of the numerical domain presented in Figure 5. Despite the high levels of vorticity of the C-pillar vortices for S_0, the overall circulation is higher for S_{40}. At X* = 0.23, $\Gamma*$ since S_{40} is 30% higher than S_0. The flow overcoming the rounded edge results in a notable 3D organization characterized by a large scale rotation around the longitudinal axis. The longitudinal rotation, as reported in Figure 6, generates a lower pressure for S_{40} with respect to S_0, which is consistent with the surface pressure measurements analyzed previously in Figure 2 relating to the local base drag increase.

To help to visualize the tridimensional flow modifications due to afterbody rounding, streamlines from numerical simulations are reported in Figure 7. Consistently with the cross-flow visualizations, it can be noticed the presence of the C-pillar vortices for the S_0 thanks to the low pressure foot-print of the vortices. The sharp side pillars force the lateral flow to separate, generating longitudinal vortices. As analyzed by the same authors,[6] it is suggested that for S_0, the sharp lateral edges "shield the wake separation region at the base and enable a "two-dimensional separation, "2D meaning that the mean streamlines at separation are more parallel to the orientation of the flow over the window, while longitudinal vorticity is concentrated in the C-pillar vortices. On the contrary, for rounded edges the flow is drawn in from the sides toward the center over the slanted surface. The separation at the base is then notably 3D for S_{40}, associated with high spanwise and vertical velocity components.

3.2 Crosswind

To gain further insight on the influence of afterbody rounding on aerodynamic performances, crosswind tests were performed. A sketch of the crosswind aerodynamic characteristic is drawn in Figure 8. In the present experiments, the yaw angle β varied from −30° to 30° and the wind tunnel speed was 40 m/s. All of the aerodynamic coefficients are scaled by the same frontal surface area as is usually done in the study of crosswind characteristic.[11] Since the model is symmetric, only the results in [−30°; 0°] are reported. The choice of such large range of angles is motivated in what follows. Due to meteorological phenomena, small angles of crosswind have a non negligible probability of exceedance. As reported by Palin et al.,[12] the majority of possible yaw angles are within the band of zero to 10 degrees, which covers more than 99% of the probability distribution. The study of this interval permits then to complete the aerodynamic performance analysis of the model. Angles in [−30°; −20°] are tested mostly for

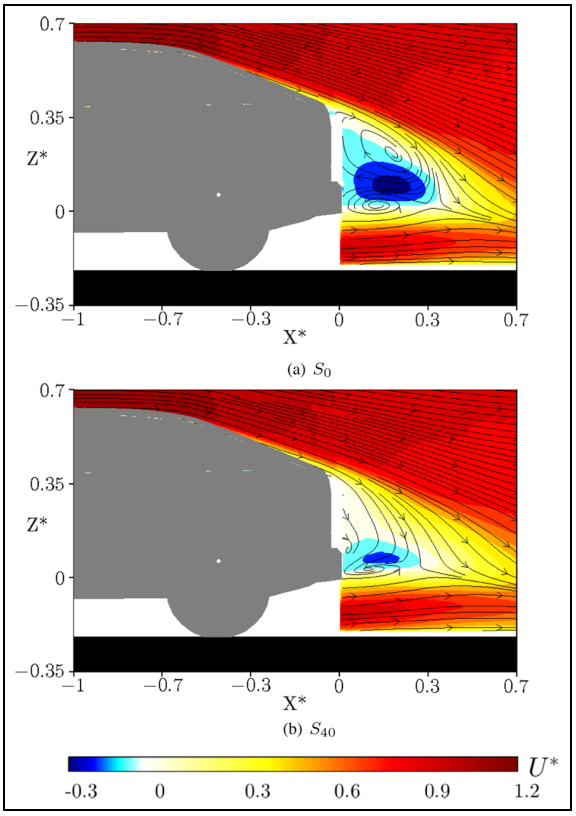

Figure 4. Time averaged streamlines and mean streamwise velocity U* at Y*=0.

safety reasons. Even though the natural probability of exceedance of such angles is extremely rare, they can occur due to driving conditions such as overtaking[13] or extreme weather conditions.[14]

The yawing moment is generated by the front and rear contribution of the side forces. It is computed by using the middle of the wheelbase and the truck as a reference. Since the modification of the side pillars radii is in the model rear end the analysis will be focused on the generation of the rear forces, i.e. Cy_{rear} and Cl_{rear}. The overall drag will be discussed as well. Figure 9 reports experimental aerodynamic coefficients in $[-30°;\ 0°]$ yaw angles. The starred coefficients are normalized by the value of S_0 at $-30°$. As a general trend, drag experiences almost a 30% increase in $[-15°;\ 0°]$. At $-5°$ and $-10°$ yaw angle S_{40} drag is respectively 3.5% and 4.5% lower compared to S_0. The drag increase due to yaw angle increasing is more important for the sharp side pillar. Moreover while drag is constant in $[-30°;\ -20°]$ for the rounded models, it continues to increase for S_0.

Since yaw angles do not have the same probability of occurrence, many authors have performed their performance analysis in terms of wind average drag coefficient as Buckley et al.[15] and Cooper[16]. Taking into account the yaw angles probability distribution proposed,[12], S_{40} averaged drag in $[-10°;\ 0°]$ which was 3% lower than S_0.

CY_{front}, not shown here, does not have important differences among the four rear ends. On the contrary, CY_{rear} experiences significant changes. S_{40} side rear

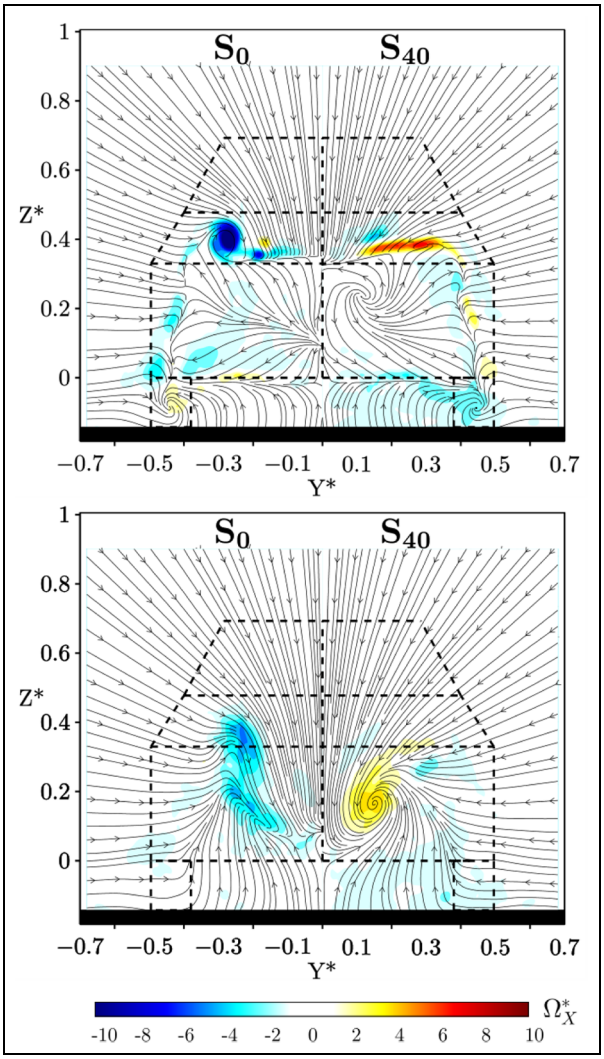

Figure 5. Mean Streamwise Vorticity Ω_{*_x}. Top X*= 0.02, bottom X*= 0.23. Left S_0, Right S_{40}.

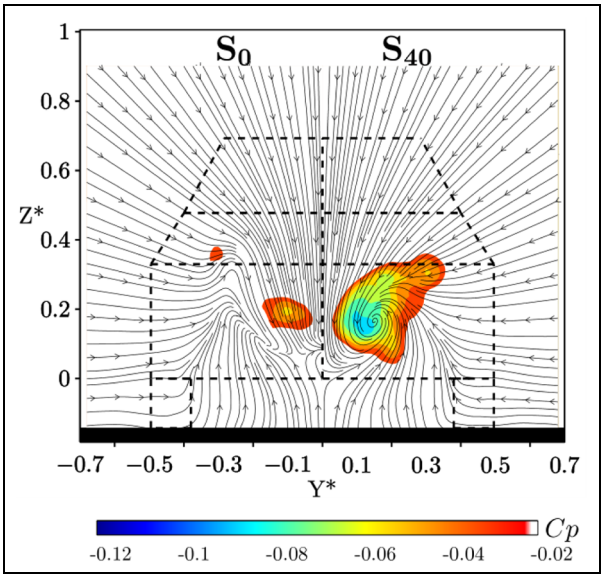

Figure 6. Mean pressure coefficient Cp at X*= 0.23. Left S_0, Right S_{40}.

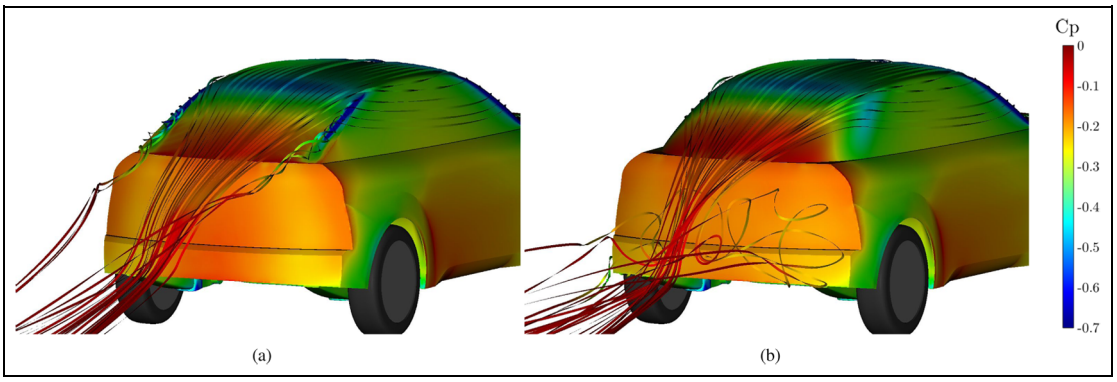

Figure 7. Time averaged streamlines from numerical simulations. The streamlines and the surface of the body are colored by the pressure coefficient C_p. (a) S_0. (b) S_{40}.

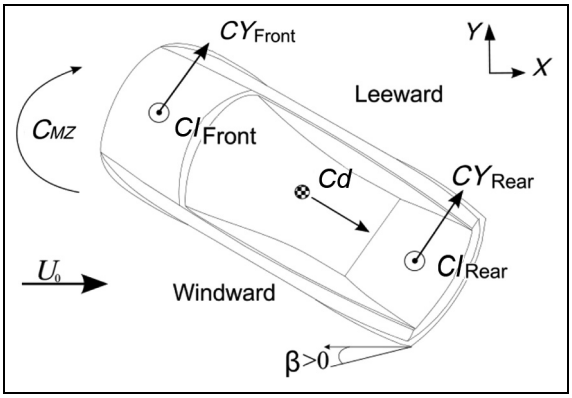

Figure 8. Sketch of the crosswind aerodynamic characteristics.

force is 20% and 30% lower than S_0 respectively at $-10°$ and $-30°$. It is important to notice that CY_{rear} acts as a counter-rotating force to the yawing moment (Figure 8). This means that, reducing the side rear force, induces the increase of the yawing moment. The value of the yawing moment CM_Z, grows with an increasing C-pillar radius. At $-30°$, S_{40} yawing moment is 21% higher than S_0. It is interesting to notice that S_8, featuring a very small side radius, resulted in a 12% CM_Z increase when compared to S_0. It results then that the yawing moment has a pronounced increase as the side edges feature a small radius.[2]

Howell et al.[17] analyzed the relationship between lift and lateral aerodynamics. According to them, when the rear lift is reduced, there is often a reduction in yawing moment. However, the use of rounded edges does not follow this pattern since the model with the lowest lift at zero yaw angle had the highest yawing moment. The rear lift in $[-10°; 0°]$ is similar to a 0° yaw angle: the S_{40} model has lower rear lift compared to S_0 due to the C-pillar vortices and their induced flow elimination over the rear window (-27% at 0° yaw angle). Interestingly, an inversion of the behavior appears for yaw angles bigger than $-15°$. The rounded models experience a sudden growth of rear lift (+ 47% at $-30°$ yaw angle) due to the flow acceleration around the rounded rear pillar, creating a strong suction on the windward side of the model.[18] On the contrary, the windward side sharp edge of S_0, promotes flow separation over the rear window, resulting in moderate growths of rear lift when compared to the rounded model. The differences in the yawing moment can be explained by the different pressure distributions over the model, reported in Figure 10.

The top view of the numerical pressure distributions at 0 yaw angle are reported to show the rear pressure characteristics. The C-pillar vortices pressure foot-prints is clearly remarked over the side sharp pillar for S_0 (Figure 10(a)). At $\beta = -30°$, C-pillar vortices disappear due to the flow separation imposed by the windward sharp edge. Strong acceleration over the windward rounded edge is visible for S_{40} thanks to the important pressure decrease over the edge (Figure 10(d)).

Side views are reported in Figures 10(e) to 10(h) to complete the pressure distribution analysis. In fact, not only the windward side, i.e. the suction over rounded C-pillar, contributes to the overall yawing moment. It is interesting to notice that, on the leeward side, the reduced pressure foot-print of the vortex generated at the forebody and the pressure recovery over the rounded C-pillar contribute to the yawing moment increase.

Figure 11 reports a horizontal pressure profile over the vehicle as in the work of Howell.[19] Those plots quantify the effects of the rear slant pressure to the yawing moment. Values outside the solid black line are negative. For S_0, the contribution to the yawing moment derives mainly from the leeward front part. Moreover, this contribution is constant for both models. For S_{40}, the windward rear side low pressure is visible due to the rear peak outside the solid black line. The differences between the two models plots underline the origin of the increased yawing moment for S_{40}.

4 Geometry modifications

4.1 Spoilers

Rear spoilers are undoubtedly efficient devices used to increase vehicles downforce in racecars.[20] Nowadays, small spoilers are used in commercial vehicles to modify

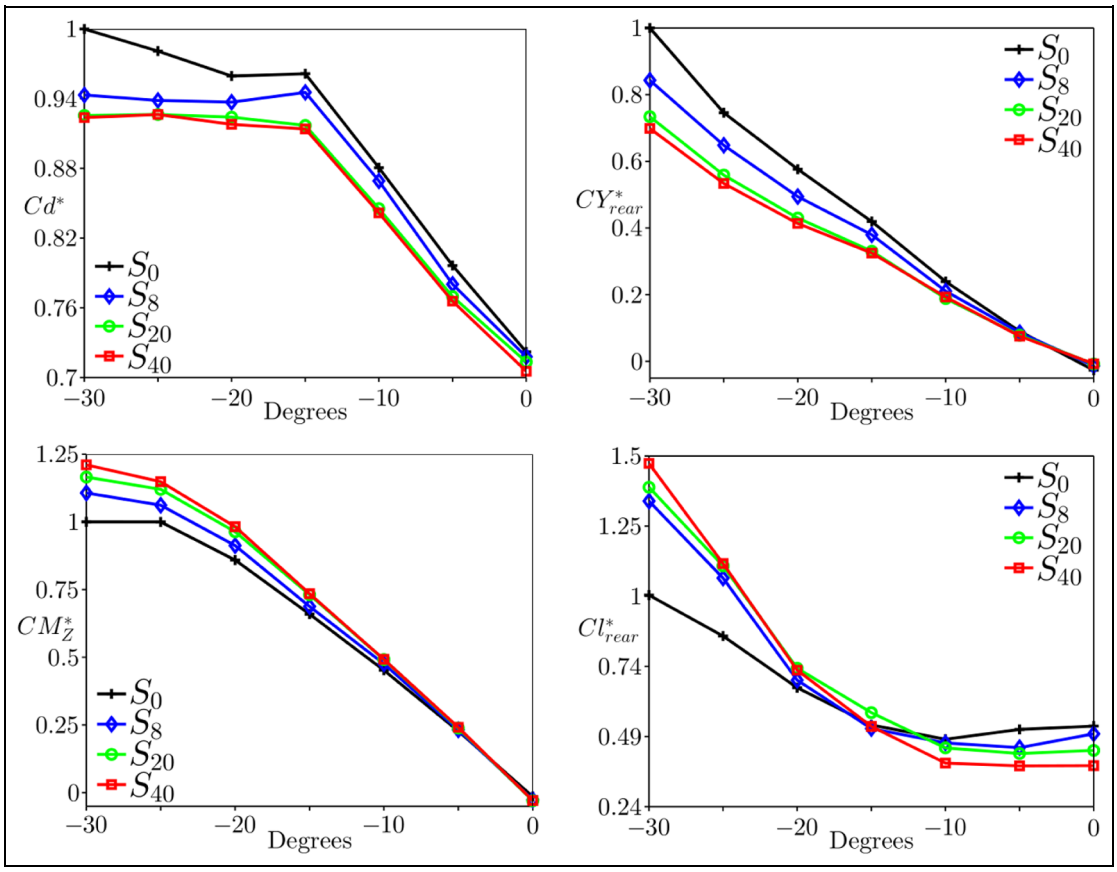

Figure 9. Normalized aerodynamic coefficients. From top to bottom: Cd^*, CY^*_{rear}, CM^*_Z, Cl^*_{rear}.

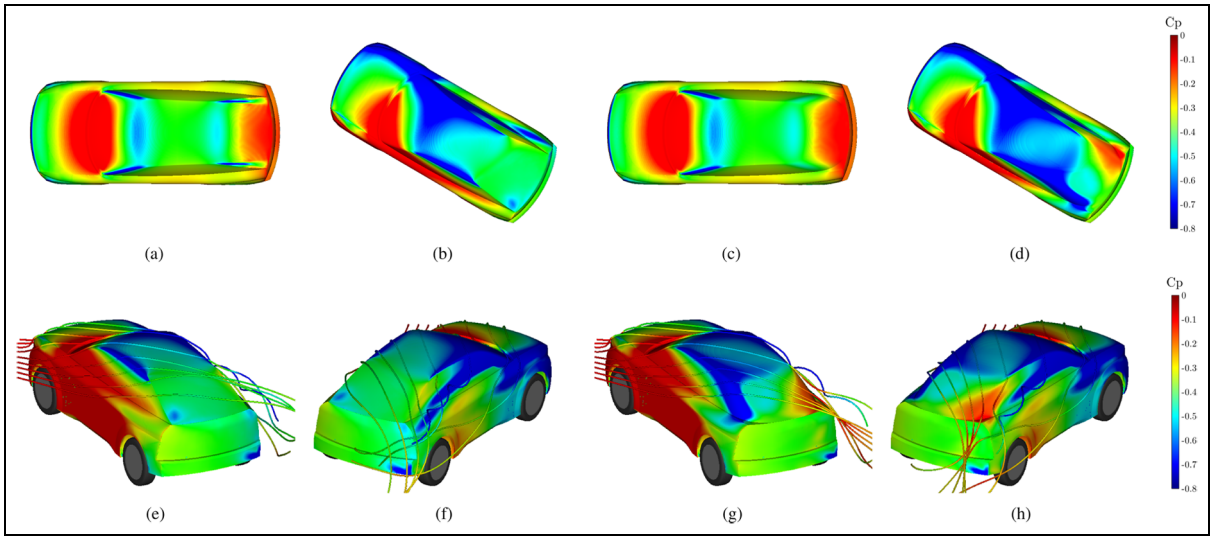

Figure 10. Surface pressure and streamlines visualizations from numerical simulations. (a) S_0 configuration at 0° yaw. (b) S_0 configuration at -30° yaw. (c) S_{40} configuration at 0° yaw. (d) S_{40} configuration at -30° yaw. (e) S_0 configuration at -30° yaw, windward side. (f) S_0 configuration at -30° yaw, leeward side. (g) S_{40} configuration at -30° yaw, windward side. (h) S_{40} configuration at -30° yaw, leeward side.

the near wake flow field. To investigate the influence of afterbody rounding on the efficiency of rear spoilers, additional experiments are presented in what follows. In this test, three different spoilers at the rear slant end were used. The size of the spoilers, their placement, and their shape are chosen by the PSA style department. In

fact, small devices that extend the rear slant line are an interesting solution for both style and aerodynamic performances. The position of the spoilers and their numbering is reported in Figure 12.

Regarding the flow modifications generated by the use of such devices a pressure recovery is expected upstream of the spoiler. It results in a rear slant drag reduction. This effect, coupled with the high pressure over the spoiler itself, contributes to the overall drag and lift reductions. The spoiler also allows for base drag reduction due to modification of the near wake close to the vehicle base. If the mechanisms associated with rear spoilers are well known and understood,[21] the interactions with the flow modifications generated by rounded side pillars have not been investigated yet.

The normalized aerodynamic coefficients relative to the different rear spoiler configurations are reported in Figure 13. They are normalized by the values of the model without a spoiler, referred to as *NoSpoiler*. *Spoiler1* generates the same drag reduction for both S_0 and S_{40}, i.e. 3.5% with respect to *NoSpoiler*. Increasing the size of the spoiler does not further reduce drag for S_0. On the contrary, S_{40} with *spoiler3*, experiences a drag reduction of up to 4.5% when compared to S_{40} without a spoiler. Regarding the relative comparison between the two models with *spoiler3*, drag is 3% lower for S_{40} when compared to S_0. As previously explained, rounding the edges resulted in a local increase of base drag. Furthermore, in the 2D analysis of the flow field, Figure 4, the shortening of the near wake, imposed by the side flow downwash, was related to the base drag increase. In terms of drag, the use of spoilers placed at the rear slant end, is then more effective when the near wake length is not optimal as for S_{40}.

Regarding the lift, *spoiler1* strongly impacts S_0 more so than S_{40}. In fact, *spoiler1* generates a 30% lift reduction for S_0 and only a 20% reduction for S_{40}. The S_0 model with *spoiler3*, experiences a lift reduction of up to 40% when compared to the same model without a spoiler. Despite this important reduction, the overall lift coefficient for S_{40} is still 15% lower than that of S_0. As a matter of fact, the lift without a spoiler for S_{40} is 27% lower than S_0 as reported in Table 2. The higher lift reduction for S_0 can be related to the presence of the C-pillar vortices due to the sharp side edges. The spoilers, promoting a pressure recovery over the rear window, directly impacts the strength of those vortices, resulting in an important lift reduction.

As a general trend, spoilers are able to reduce the negative local effects generated by the side pillar edges. They are then more efficient in terms of drag reduction for models with rounded rear edges. Regarding the lift, spoilers are suitable passive devices to improve lift reduction for sharp rear edge models.

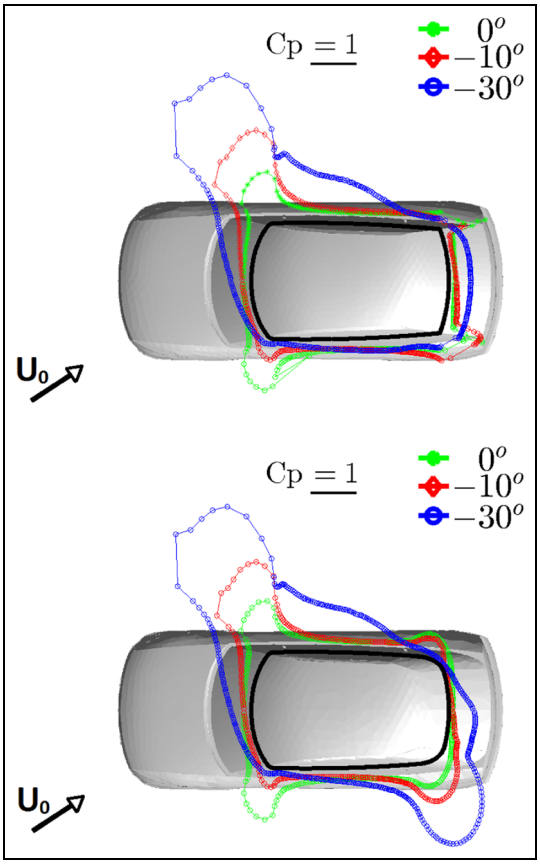

Figure 11. Pressure distribution at Z* = 0.43: Top S_0, Bottom S_{40}. Values outside the solid black line correspond to negative pressure coefficient.

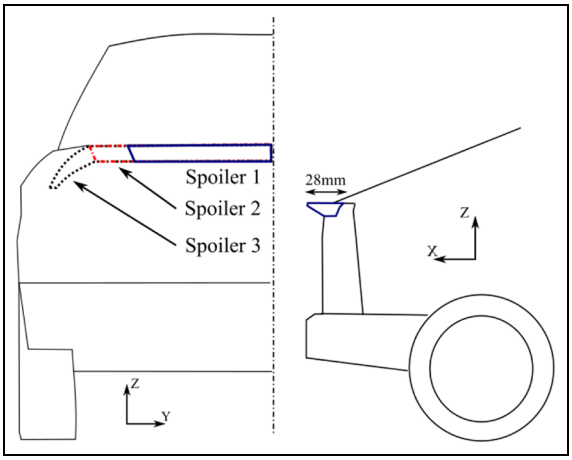

Figure 12. Spoilers location over the model. Spoiler2 includes spoiler1 and spoiler3 includes spoiler2.

4.2 Diffuser

An interbody diffuser is commonly used in racing cars to develop large downforce. Recently, diffusers have become a good strategy for drag and lift reduction even for passenger cars.[22] Three different mechanisms contribute to produce high levels of downforce and drag reduction in a passenger car. The first mechanism is due to the ground interaction. By placing the body in ground proximity, the acceleration of the flow underneath the body will reduce the underbody pressure resulting in a downforce (i.e. negative lift).[23] The

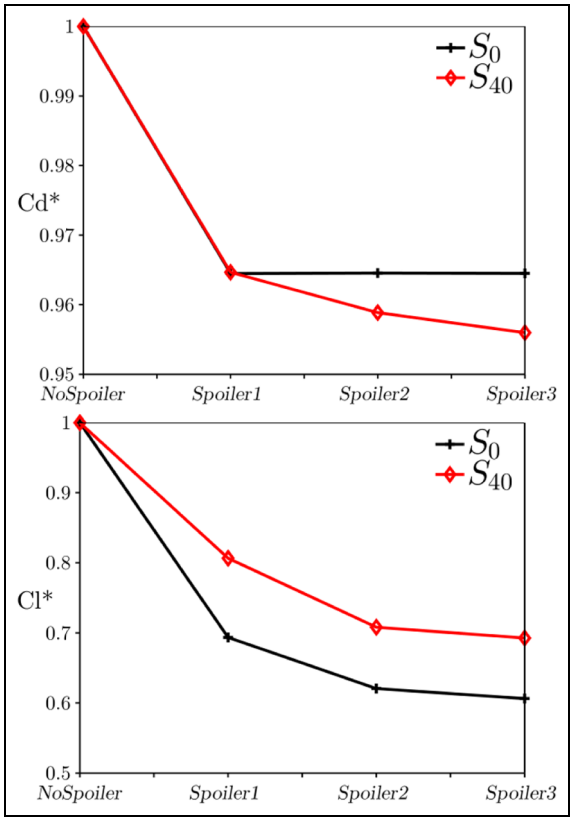

Figure 13. Normalized aerodynamic coefficients for the different rear spoiler configurations. Top: drag coefficient, bottom: lift coefficient.

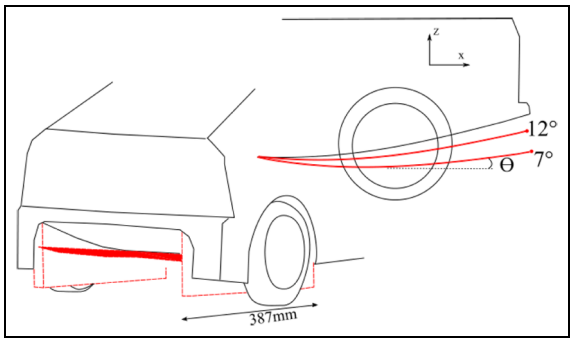

Figure 14. Schematics of the underbody diffuser. The side view in the top shows the maximum and minimum diffuser angles tested.

second mechanism generating downforce is related to the upsweep of the rear underbody. The angle of the diffuser will camber the flow resulting in a local pressure reduction around the diffuser edge. The last principle, is commonly referred to as "diffuser pumping". As the ratio of the inlet to outlet area increases, pressure recovery is performed in the diffuser area. Given that the near wake pressure remains constant, the pressure upstream to the diffuser decreases and the underbody flow rate increases. These effects result in a further decrease in underbody pressure, which produces the "pumping down".[24]

The diffuser used in these experimental tests was produced by means of 3D printer. A flat underbody was used here instead of the realistic underbody used for the previous tests. The underbody featured already a diffuser angle of $\Theta = 15$ degrees. The schematics of the underbody diffuser are drawn in Figure 14. The underbody used was made from a thin cambered plate reproducing the original diffuser shape. Its angle variation had several limitations. Since the original diffuser was not flat but featured a convex shape, reducing the angle Θ increased the frontal surface of the model. For that reason, the minimum angle tested was 7 degrees which results in a frontal area variation of approximately 2%. All of the aerodynamic coefficients are rescaled to take into account the area variation. Moreover the maximum angle was limited to 12 degrees due to the hinge limitation of the diffuser. The diffuser was fitted with side plates as in the works of Cooper et al.[25] to prevent the flow from overcoming the side of the diffuser and to provide fixation for the diffuser sides.

The starred aerodynamic coefficients are normalized by the value at 7 degrees for each model. Drag evolution for the diffuser's angles variation is reported in the top of Figure 15. The diffuser's drag reduction is the same for both models.

Increasing the diffuser angle, from 7 to 12 degrees, results in drag reduction up to 10% for both models. At 12 degrees, S_{40} had a drag 1.5% lower than S_0. This is consistent with the base geometry trends reported in Table 2. The averaged base pressure, reported in the center of Figure 15, increases as well for larger diffuser angles, in accord with the drag reduction. It is quite striking to notice how the plots are "parallel". The gap between the lines seems to be imposed by the side radius and remain constant for all diffuser angles.

The bottom of Figure 15 reports the lift evolution. As expected by the use of the diffuser, increasing its angle results in downforce, i.e. lift reduction. The lift for both models is canceled out. The lift reduction is the same for both models from 7 to 9 degrees. For diffuser angles greater than 9 degrees the lift reduction is more effective for the rounded model. For S_{40}, the upsweep of the diffuser should make the wake more symmetrical with respect to the flow structures organization reported in Figure 4. For S_0, since the reference wake was already symmetric, it is suggested that a high diffuser angle tends to break the symmetry for S_0 resulting in a wake directed upwards. It could explain that high diffuser angles for S_0 has a moderate lift reduction with respect to S_{40}.[22]

5 Conclusions

Experimental and numerical analyzes were used to study the influence of afterbody rounding on the aerodynamic characteristics of a fastback vehicle model. At zero crosswind, rounded edges resulted having a minimal impact on drag due to opposite effects over the

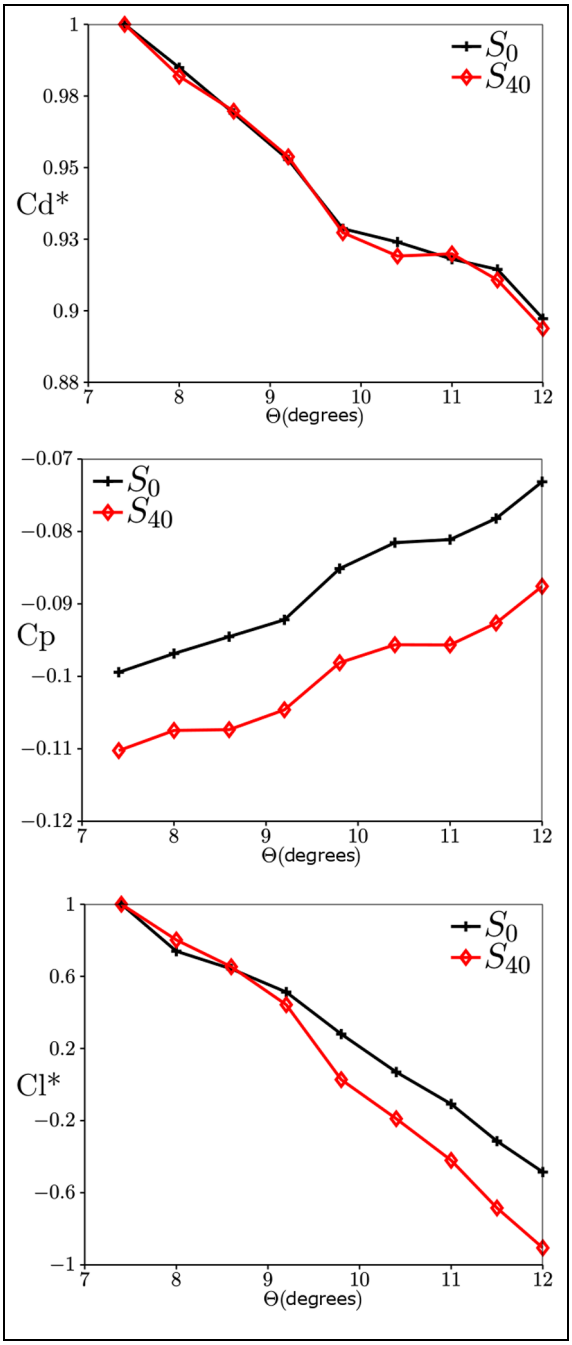

Figure 15. Normalized aerodynamic coefficients for underbody diffuser angles variation. Top: drag coefficient, center: averaged base pressure, bottom: lift coefficient.

rear slant and the base. Important lift reductions were achieved thanks to the elimination of the C-pillar vortices. The impact of rounded edges on the near wake organization due to the different longitudinal vorticity distribution was highlighted. Unfortunately, rounded edges resulted in a detriment of the lateral stability, generating a severe increase of yawing moment and rear lift. Geometry modifications were also tested to study their efficiency variation due to side rounding. Spoilers resulted to recover the negative base drag effects of side rounding. The lift reduction was much more effective for a sharp rear edge. Regarding the use of diffuser, the overall drag modifications due to diffuser angles variations were not sensitive to afterbody rounding. Lift force is found to be more sensitive to high diffuser angles for the rounded edge model.

This analysis helps for future vehicles efficient design giving the overall aerodynamic behavior of afterbody rounding. Innovative design should take into account the right balance between sharp and rounded edge since they have different performances with respect to yaw angles. Additional tests should be performed to study the effects of a non-constant side radius to find an optimal compromise in terms of drag, lift, and lateral stability.

Acknowledgements

The authors are thankful to B. Tixier from the Exa company for performing the numerical simulations and to Y. Goraguer, the wind tunnel manager, for his time and efforts during the experimental tests. We acknowledge the PSA designer Yong Wook Sin for the fruitful collaboration.

This work has been performed in the framework of the "OpenLab Fluidics @Poitiers.

Declaration of conflicting interests

The author(s) declared no potential conflicts of interest with respect to the research, authorship, and/or publication of this article.

Funding

The author(s) disclosed receipt of the following financial support for the research, authorship, and/or publication of this article: The present work results from a CIFRE agreement between the École Nationale Supérieure de Mécanique et d'Aérotechnique (ENSMA) and the research and innovation department of fluid mechanics of PSA Gropue.

References

1. Gilhaus AM and Renn VE. Drag and driving-stability-related aerodynamic forces and their interdependence-results of measurements on 3/8-scale basic car shapes. SAE Technical Paper No. 860211, 1986.
2. Howell JP. Shape features which influence crosswind sensitivity, vehicle ride and handling conference. *I Mech E Paper C466/036/93*, 1993.
3. Thacker A, Aubrun S, Leroy A et al. Effects of suppressing the 3D separation on the rear slant on the flow structures around an Ahmed body. *J Wind Eng Ind Aerod* 2012; 107: 237–243.
4. Fuller J and Passmore MA. The importance of rear pillar geometry on fastback wake structures. *J Wind Eng Ind Aerod* 2014; 125: 111–120.
5. Palin R, Johnston V, Johnson S et al. The aerodynamic development of the Tesla model S-Part 1: Overview. SAE Technical Paper No. 2012-01-0177, 2012.

6. Rossitto G, Sicot C, Ferrand V et al. Influence of afterbody rounding on the pressure distribution over a fastback vehicle. *Exp Fluids* 2016; 57(3): 1–12.
7. Benedict L and Gould R. Towards better uncertainty estimates for turbulence statistics. *Exp Fluids* 1996; 22(2): 129–136.
8. Fares E. Unsteady flow simulation of the Ahmed reference body using a lattice Boltzmann approach. *Comput Fluids* 2006; 35(8): 940–950.
9. Duncan BD, Sengupta R, Mallick S et al. Numerical simulation and spectral analysis of pressure fluctuations in vehicle aerodynamic noise generation. SAE Technical Paper No. 2002-01-0597, 2002.
10. Rossitto G, Sicot C, Ferrand V et al. Wake structure and drag of vehicles with rounded rear edges. In: *50th edition of the International Conference on Applied Aerodynamics*, Toulouse, France, 30 March–01 April 2015, p.1.
11. Hucho WH and Sovran G. Aerodynamics of road vehicles. *Annu Rev Fluid Mech* 1993; 25(1): 485–537.
12. D'Hooge A, Palin R, Rebbeck L, et al. Alternative simulation methods for assessing aerodynamic drag in realistic crosswind. *SAE Int J Passeng Cars - Mech Syst* 2014; 7(2): 617–625.
13. Noger C, Regardin C and Szechenyi E. Investigation of the transient aerodynamic phenomena associated with passing maneuvers. *J Fluids Struct* 2005; 21(3): 231–241.
14. Baker C and Reynolds S. Wind-induced accidents of road vehicles. *Accid Anal Prev* 1992; 24(6): 559–575.
15. Buckley FT and Sekscienski WS. Comparisons of effectiveness of commercially available devices for the reduction of aerodynamic drag on tractor-trailers. SAE Technical Paper No. 750704, 1975.
16. Cooper KR. Truck aerodynamics reborn: Lessons from the past. *SAE Trans* 2003; 112(2): 132–142.
17. Howell J and Fuller JB. A relationship between lift and lateral aerodynamic characteristics for passenger cars. SAE Technical Paper No. 2010-01-1025, 2010.
18. Cairns RS. Lateral aerodynamic characteristics of motor vehicles in transient crosswinds. *Report, Cranfield University, UK*, 1994.
19. Howell J. The side load distribution on a Rover 800 saloon car under crosswind conditions. *J Wind Eng Ind Aerod* 1996; 60: 139–153.
20. Katz J. Aerodynamics of race cars. *Annu Rev Fluid Mech* 2006; 38: 27–63.
21. Fukuda H, Yanagimoto K, China H et al. Improvement of vehicle aerodynamics by wake control. *JSAE Rev* 1995; 16(2): 151–155.
22. Marklund J, Lofdahl L, Danielsson H et al. Performance of an automotive under-body diffuser applied to a sedan and a wagon vehicle. *SAE Int J Pass Cars Mech Sys* 2013; 6(1): 293–307.
23. Barlow JB, Guterres R and Ranzenbach R. Experimental parametric study of rectangular bodies with radiused edges in ground effect. *J Wind Eng Ind Aerod* 2001; 89(14): 1291–1309.
24. Cooper KR, Bertenyi T, Dutil G et al. The aerodynamic performance of automotive underbody diffusers. SAE Technical Paper No. 980030, 1998.
25. Cooper KR, Syms J and Sovran G. Selecting automotive diffusers to maximise underbody downforce. SAE Technical Paper No. 2000-01-0354, 2000.